nature materials

ARTICLES

PUBLISHED ONLINE: 6 SEPTEMBER 2009 | DOI: 10.1038/NMAT2526

One-dimensional imidazole aggregate in aluminium porous coordination polymers with high proton conductivity

Sareeya Bureekaew[1,2], Satoshi Horike[1,2], Masakazu Higuchi[1], Motohiro Mizuno[3], Takashi Kawamura[1], Daisuke Tanaka[1], Nobuhiro Yanai[1] and Susumu Kitagawa[1,2,4]*

The development of anhydrous proton-conductive materials operating at temperatures above 80 °C is a challenge that needs to be met for practical applications. Herein, we propose the new idea of encapsulation of a proton-carrier molecule—imidazole in this work—in aluminium porous coordination polymers for the creation of a hybridized proton conductor under anhydrous conditions. Tuning of the host–guest interaction can generate a good proton-conducting path at temperatures above 100 °C. The dynamics of the adsorbed imidazole strongly affect the conductivity determined by ^{2}H solid-state NMR. Isotope measurements of conductivity using imidazole-d_4 showed that the proton-hopping mechanism was dominant for the conducting path. This work suggests that the combination of guest molecules and a variety of microporous frameworks would afford highly mobile proton carriers in solids and gives an idea for designing a new type of proton conductor, particularly for high-temperature and anhydrous conditions.

Anhydrous proton-conducting solids that are able to operate at high temperature (~120 °C) are required in fuel-cell technology[1,2]. Heterocyclic organic molecules such as imidazole or benzyl imidazole have attracted considerable attention for this purpose because they are non-volatile molecules with high boiling points and they can exist in two tautomeric forms with respect to a proton that moves between the two nitrogen atoms, which supports a proton-transport pathway[3,4]. The protonic defect may cause local disorder by forming protonated and unprotonated imidazoles. In such materials, the proton transport may occur through structure diffusion that involves proton transfer between the imidazole and the imidazolium ion through the hydrogen-bonded chain, including the molecular reorientation process for subsequent intermolecular proton transfer[1]. Theoretically, the magnitude of the ionic conductivity is given as

$$\sigma(T) = \sum n_i q_i \mu_i$$

where n_i is the number of carriers and q_i and μ_i are the charge and mobility of the carriers, respectively[5]. Both a large amount and a high mobility of ion carriers are required to provide good proton conductivity. Hence, it is important to find suitable materials that meet these requirements. For instance, solid imidazole has a low conductivity (~10^{-8} S cm^{-1}) at ambient temperature[6] although the imidazole density (n_i) is adequately high. This is because the dense packing of imidazole, with strong hydrogen bonding in the solid state, decreases the mobility of each molecule (μ_i).

The main goal of proton-conductor modification should therefore be an improvement of the mobility of proton carriers. It is known that local and translational motion of proton carriers strongly affect the proton-transfer rate[1]. To control the mobility of proton carriers, further support matrices such as flexible organic polymers or high-porosity solids that afford space in which the carrier can move are considered promising.

Porous coordination polymers (PCPs) or metal organic frameworks constructed from transition-metal ions and organic ligands have received much attention over the past few years because of their promising applications, such as in gas storage[7–11], separation[12–17], catalysis[18–26] and conductivity[27–29]. Recent developments in approaches to combine PCP frameworks and functional guests such as polymers[30,31], metals[22,32–34] or small organic molecules[35–37] on a molecular scale have prompted us to create hybrid materials with unusual performance on the basis of the feature that crystalline nanochannels can afford a unique assembly field for functional guests with specific host–guest interactions. The guests in the nanospace of PCPs show unusual behaviour compared with in the bulk phase because each manner of assembly is heavily dependent on the nature of the PCP channels, such as their size, shape and chemical environment. Hence, we propose the use of PCPs for incorporation with proton-carrier molecules because they can provide desirable working space for carrier molecules, with high mobility and show an appropriate packing structure, for improved proton conductivities at high temperatures and under anhydrous conditions (Fig. 1).

Here, we focused on two types of PCP with one-dimensional (1D) channels and high thermal stability (~400 °C) and imidazole as the guest proton-carrier molecule. Taking the size and shape of imidazole (4.3 × 3.7 Å^2) into consideration, we chose to use the aluminium compounds [Al(μ_2-OH)(1,4-ndc)]$_n$ (**1**; 1,4-ndc : 1,4-naphthalenedicarboxylate; ref. 38) and [Al(μ_2-OH)(1,4-bdc)]$_n$ (**2**; 1,4-bdc : 1,4-benzenedicarboxylate; refs 9, 39), both of which have pore dimensions of about 8 Å, but different pore shapes and

[1]Department of Synthetic Chemistry and Biological Chemistry, Graduate School of Engineering, Kyoto University, Katsura, Nishikyo-ku, Kyoto 615-8510, Japan, [2]ERATO Kitagawa Integrated Pores Project, Japan Science and Technology Agency (JST), Kyoto Research Park building #3, Shimogyo-ku, Kyoto 600-8815, Japan, [3]Department of Chemistry, Graduate School of Natural Science and Technology, Kanazawa University, Kanazawa 920-1192, Japan, [4]Institute for Integrated Cell-Material Sciences (iCeMS), Kyoto University, Yoshida, Sakyo-ku, Kyoto 606-850, Japan.
*e-mail: kitagawa@sbchem.kyoto-u.ac.jp.

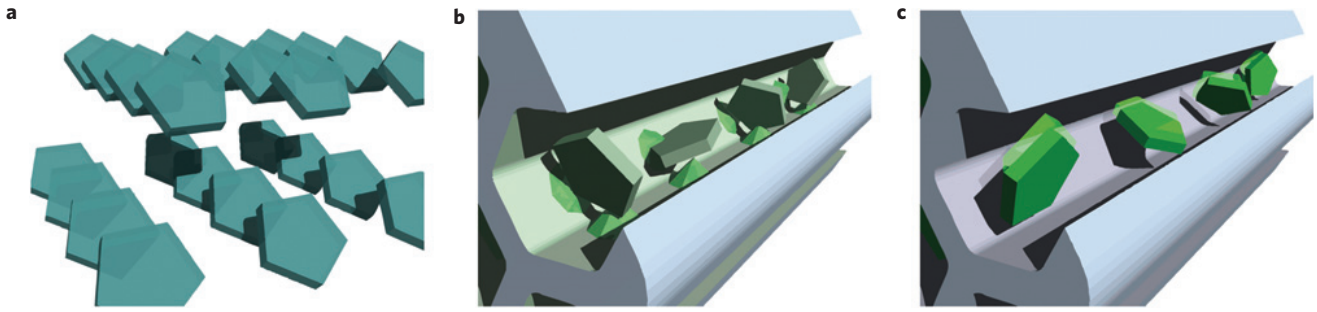

Figure 1 | Imidazole molecules are densely packed with a low mobility that adversely affects the proton-transport process. a, This occurs in the bulk solid. **b**, Imidazole accommodated in a nanochannel containing the active site with a high affinity to imidazole. The strong host–guest interaction retards the mobility of imidazole to afford the low proton conductivity. **c**, Imidazoles are accommodated in a nanochannel without strong host–guest interaction, and therefore, the molecules obtain the high mobility to show high proton conductivity.

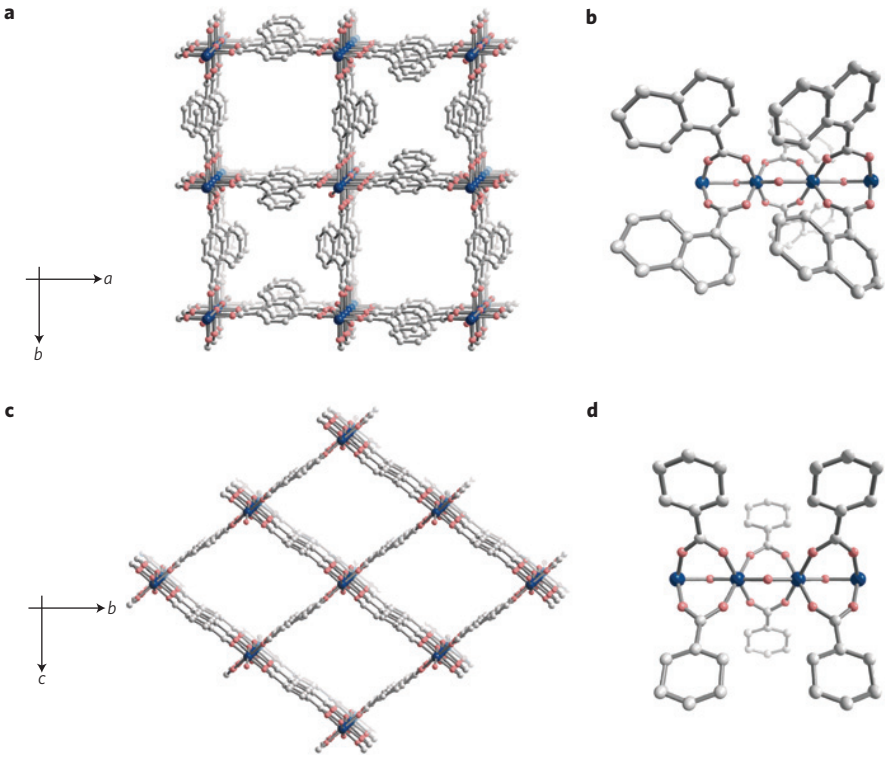

Figure 2 | Aluminium porous frameworks serving as host frameworks for the preparation of proton-conductive materials. a–d, 3D structures of **1** (**a**) and **2** (**c**) and a comparison of the ligand size effect (**b**,**d**). Al, C and O are represented as blue, grey and red, respectively. H atoms are omitted for clarity.

surface potentials and installed imidazole in each host material. We found that the nanochannels potentiated the different packing of imidazole, compared with the bulk solid imidazole. Conductivity measurements for each of the PCP–imidazole composites at various temperatures and under anhydrous conditions exhibited different profiles because of the different characteristics of the channels of the respective PCPs, resulting in different host–guest interactions, and **1** ⊃ Im had a conductivity of 2.2×10^{-5} S cm^{-1} at 120 °C. We investigated the behaviour of absorbed imidazole in the micropores by means of the solid-state NMR technique and succeeded in determining a good correlation between the features of the host channels, guest mobility and proton conductivity.

Structural information of 1 and 2

The structures of **1** and **2** comprise an infinite number of chains of corner-sharing $AlO_4(\mu_2\text{-}OH)_2$ interconnected by the dicarboxylate ligand, resulting in a 3D framework containing 1D channels. The guest-free structures of **1** and **2** are shown in Fig. 2. Crystallographic structures show that the pore surfaces of **1** and **2** are composed of hydrophobic (aromatic naphthalene and benzene ring) and hydrophilic ($AlO_4(\mu_2\text{-}OH)_2$) parts. The principal difference between the two aluminium frameworks arises from the difference in ligands 1,4-ndc and 1,4-bdc. As a result of the asymmetric bridging ligand, **1** consists of two kinds of rectangular channel with dimensions of 7.7×7.7 Å^2 and 3.0×3.0 Å^2 running along the *c* axis (Fig. 2a). This compound shows the property of a rigid framework. Figure 2b shows that steric hindrance arising from the bulky naphthalene ring of the 1,4-ndc ligand of **1** induces restriction of interaction between the polar guest molecule and μ_2-OH and/or the carboxylate group of the framework. As a result of the absence of an accessible hydrophilic pore surface, the hydrophobic character from the aromatic part of the naphthalene ring of the ligand is dominant. In other words, **1** provides two types of microchannel with hydrophobic pore surfaces.

In the case of **2**, the framework exhibits only 1D diamond-shaped channels composed of the smaller benzene moieties of 1,4-bdc, with

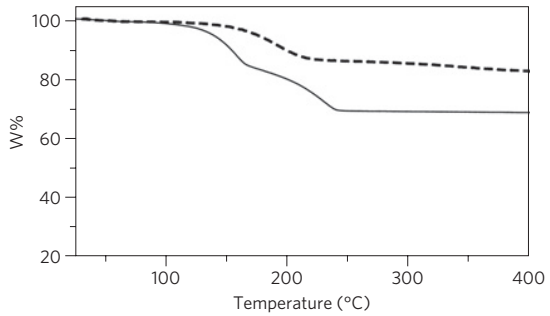

Figure 3 | Thermogravimetric curves for 1 ⊃ Im and 2 ⊃ Im over the temperature range from 25 to 400 °C at a heating rate of 10 °C min^{-1} under a N_2 atmosphere. Dashed line: **1** ⊃ Im; solid line: **2** ⊃ Im. The guest release of **1** ⊃ Im occurs in one single step that indicates the homogeneous installation of imidazole in **1**, whereas that of **2** ⊃ Im occurs in two steps, indicating two types of imidazole (which strongly and weakly interact with **2**).

dimensions 8.5 × 8.5 Å^2, running along the *a* axis. Eventually, the polar sites on the surface are exposed to guest molecules, which enhances guest-induced structural transformation of **2**, with the aid of the interaction between the imidazoles and μ_2-OH and/or a carboxylate group[40]. Thus, it is intriguing that a simple modification on the organic moiety produces channels with different nature, hydrophobic and hydrophilic for **1** and **2**, respectively[39].

Properties of the inclusion compounds

The thermogravimetric profiles of **1** ⊃ Im and **2** ⊃ Im are shown in Fig. 3. Note that **1** ⊃ Im and **2** ⊃ Im indicate the imidazole hybrid compound of **1** and **2**, respectively. The existence of imidazole in **1** and **2**, without any reactions/conversion, was confirmed by thermogravimetry/mass spectrometry. The thermogravimetric profile of **1** ⊃ Im shows 14% weight imidazole loading or 0.6 imidazole/1 Al ion. The release of accommodated imidazole commences at 160 °C and is complete at 225 °C. In the case of **2**, the loaded imidazole amounts to 30% weight or 1.3 imidazole/1 Al ion, which is twice as much as in **1**. The thermogravimetric curve shows that the loss of imidazole molecules in **2** ⊃ Im occurs in two steps: in the first step, the release of imidazole commences at 130 °C and is completed by approximately 160 °C and in the second step it commences at 160 °C and is completed by 240 °C. The percentage of imidazole loss in the first step is 50%, followed by a residual amount in the second step.

The one single-step mass loss in **1** ⊃ Im is indicative of uniformly accommodated imidazole molecules. On the other hand, on the basis of the thermogravimetric curve of **2** ⊃ Im, there are two types of imidazole molecule installed in the channel. According to the amphiphilic nature of the surface of the channel, the imidazoles with a strong interaction with the hydrophilic sites of a μ_2-OH or a carboxylate group are released at a higher temperature (160–240 °C), correlated to the weight loss in the second step, whereas the imidazoles that have less interaction with the pore surface are removed in the first step (below 160 °C).

The crystal structures of **1** and **2** (Fig. 2) reveal the following. Compound **1** consists of two types of 1D channel, namely small channels with dimensions 3.0 × 3.0 Å^2 in which imidazole is unable to be installed: only large channels with dimensions of 7.7 × 7.7 Å^2 can install the guest. Compared with **2** ⊃ Im, half the amount of accommodating imidazole per one Al is reasonable from crystal structures.

Considering that the dispersion of imidazole is uniform in the crystalline channel we could calculate the density of imidazole in the larger channels of **1** (443 Å^3) and channels of **2** (750 Å^3). This was calculated from the void space of the guest-free state by using the PLATON software package[41]. The values were about 0.15 and 0.19 g cm^{-3}, respectively. However, as the structure of **2** changes after accommodation of imidazole, it is difficult to determine the density of imidazole in **2** ⊃ Im. The densities of imidazoles in **1** ⊃ Im and **2** ⊃ Im are much smaller than that of solid bulk imidazole, which is 1.23 g cm^{-3} at ambient temperature[42]. This evidence indicates that the behaviours of imidazoles loaded to the framework considerably differ from bulk imidazole resulting from the space effect.

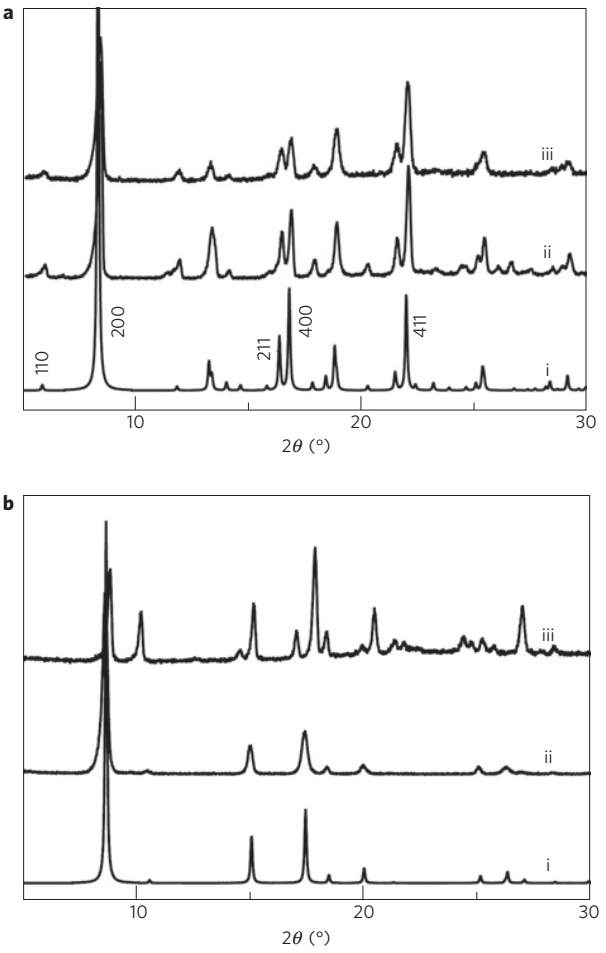

Figure 4 | Difference in flexibility of host frameworks 1 and 2 by imidazole inclusion. a, XRPD patterns of simulated **1**·2H_2O (i), **1** (ii) and **1** ⊃ Im (iii). The patterns before and after accommodation of imidazole are identical. **b**, XRPD patterns of simulated **2** (i), **2** (ii) and **2** ⊃ Im (iii). A change in the XRPD patterns after accommodation of imidazole is observed[39].

The X-ray powder diffraction (XRPD) patterns shown in Fig. 4 show that the diffraction pattern of **1** ⊃ Im is the same as that of apohost **1**, corresponding to the robustness of **1**. Conversely, the peak positions and pattern of **2** ⊃ Im are different from those of apohost **2** and the shrinkage after installation of imidazole is observed. This is because of strong interaction between the polar imidazole and the hydrophilic pore surface of the flexible **2**.

Conductivity of 1 ⊃ Im and 2 ⊃ Im

We aimed to achieve proton conductivity at temperatures around 100 °C and hence to design composites that are stable at the target temperatures. We already confirmed that the prepared composites **1** ⊃ Im and **2** ⊃ Im are stable up to 130 °C without any loss using thermogravimetry. Conductivities of **1** ⊃ Im and **2** ⊃ Im were measured by a.c. impedance spectroscopy, which is a versatile

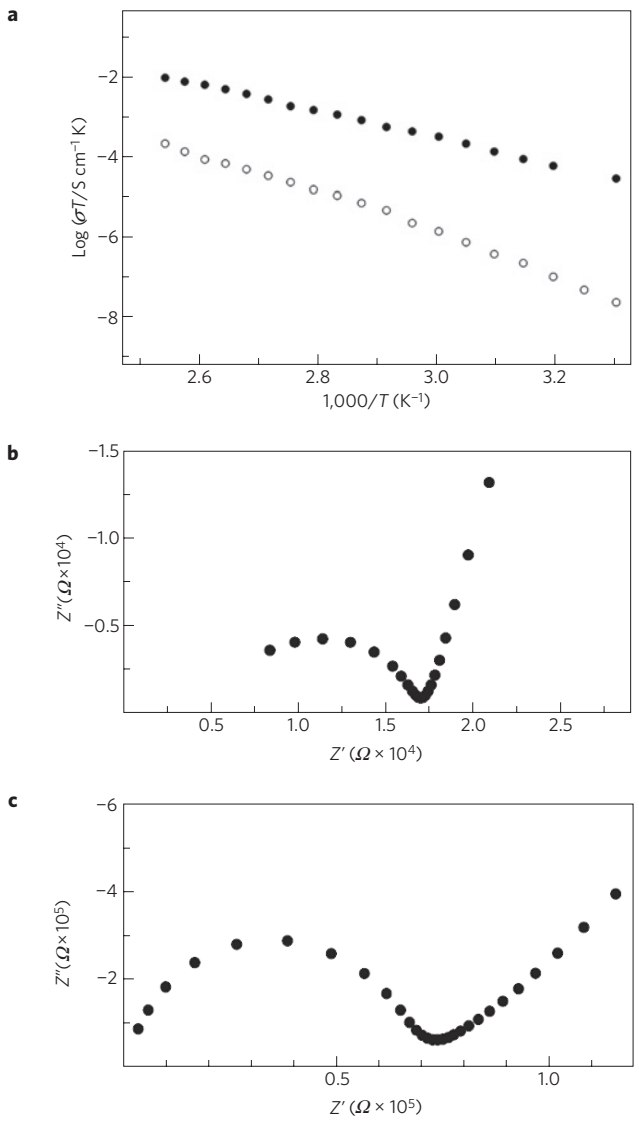

Figure 5 | Temperature dependencies of proton conductivity of 1 and 2 with imidazole molecules. a, Proton conductivity of **1** ⊃ Im (filled circles) and **2** ⊃ Im (open circles) under anhydrous conditions determined by an a.c. impedance analyser. **b**,**c**, Nyquist diagrams of **1** ⊃ Im (**b**) and **2** ⊃ Im (**c**) at a temperature of 120 °C.

electrochemical tool to characterize intrinsic electrical properties of materials. Figure 5b,c shows Nyquist plots (Z' versus Z'') of the complex impedance measured on **1** ⊃ Im and **2** ⊃ Im under a nitrogen atmosphere at 120 °C. The impedance plots of the two complexes are typical of materials with predominant ionic conductivity. They show one semicircle with a characteristic spur at low frequencies, which indicates blocking of H^+ ions at the gold electrodes. The magnitude of Z' decreased with an increase in temperature. The conductivity of the samples was calculated from the impedance value using the following equation

$$\sigma = \frac{L}{Z \cdot A}$$

where σ is the conductivity (S cm^{-1}), L is the measured sample thickness (cm), A is the electrode area (cm^2) and Z is the impedance (Ω).

The temperature dependence of proton conductivities of **1**, **1** ⊃ Im and **2** ⊃ Im, measured under anhydrous conditions at temperatures ranging from 25 to 120 °C, are shown in Fig. 5a. Guest-free **1** shows a conductivity lower than 10^{-13} S cm^{-1}, confirmed by d.c. measurement, which is indicative of negligible proton conductivity for this apohost framework. After installation of imidazole, the proton conductivity of **1** ⊃ Im is 5.5×10^{-8} S cm^{-1} at room temperature. Although the mole fraction of imidazole in **1** ⊃ Im is much smaller than that of bulk imidazole, the proton conductivity of **1** ⊃ Im is of the same order as that of solid bulk imidazole. This is possibly because of the effect of the nanospace on the dynamic motion of imidazole. The proton conductivity of **1** ⊃ Im improves significantly as the temperature increases: at 120 °C the proton conductivity reaches 2.2×10^{-5} S cm^{-1}. Note that bulk imidazole at this temperature is no longer in the solid phase. This increase in the temperature-dependent conductivity of **1** ⊃ Im, compared with the conductivity profile of apohost **1**, indicates that a significant improvement in the conductivity arises directly from the accommodated imidazole. Furthermore, the conductivity of **1** ⊃ Im continuously increases with an increase in temperature with the activation energy of 0.6 eV. This result indicates that phase transition does not take place. The mobile imidazole induces high-temperature (>100 °C) proton conductivity in **1** ⊃ Im. We can improve the mobility of imidazole by taking advantage of the isolating effect of PCPs. The evidence from the isotope effect (see Supplementary Fig. S1) shows that the proton conductivity of our systems is mainly contributed by the proton-hopping mechanism.

To improve the proton conductivity we increased the amount of loaded imidazole (the number of charge carriers, n_i) by using **2**, which has twice the amount of accessible space for imidazole as the supporting framework. However, the proton conductivity of **2** ⊃ Im at ambient temperature is about 10^{-10} S cm^{-1}, which is lower than that of **1** ⊃ Im. As in the case of **1** ⊃ Im, the conductivity of **2** ⊃ Im increases as the temperature increases with the activation energy of 0.9 eV and it reaches 1.0×10^{-7} S cm^{-1} at 120 °C. The proton conductivity of **2** ⊃ Im is about two orders of magnitude lower than that of **1** ⊃ Im, although the amount of loaded imidazole is higher than that of **1** ⊃ Im. This is also possibly because of the difference in dynamic motion of the guest, which is based on the interaction between the guest and the host. Microchannels in compound **1** have a nonpolar potential surface and polar imidazole does not interact strongly with the host framework; therefore, it can move freely in this channel. Nonetheless, in the case of the polar-surface microchannels in **2**, the half amount of imidazole interacts strongly with the hydrophilic sites of the host framework. The strong host–guest interactions give rise to the shrinkage of the framework, eventually to a unit cell, resulting in the different environments for imidazole accommodated in **2**, compared with in **1**. Therefore, because of strong host–guest interaction and dense packing, the imidazoles with strong interaction with the μ_2-OH and/or the carboxylate group of **2** are not allowed to move or rotate freely in the framework. Consequently, the conductivity in **1** ⊃ Im is larger than in **2** ⊃ Im.

Direct observation of dynamics of imidazoles

Solid-state ^{2}H NMR spectroscopy is suitable for examining the dynamics of target molecules selectively[43–45]. We therefore used this analytical technique to determine the mobility and its correlation with the conductivity of adsorbed imidazole in **1** and **2**. The ^{2}H NMR powder line shapes are sensitive to local molecular motion and are characterized in terms of both the timescale and the mode of the motion, such as rotation or wobbling behaviour[46,47]. We introduced imidazole-d_4 for each host instead of non-deuterated imidazole and checked that the adsorbed amount for each guest was identical to that in the normal hosts. The ^{2}H NMR spectra of **1** ⊃ Im and **2** ⊃ Im recorded at different temperatures are shown in Fig. 6. In the case of **2** ⊃ Im (Fig. 6, right), at the lowest

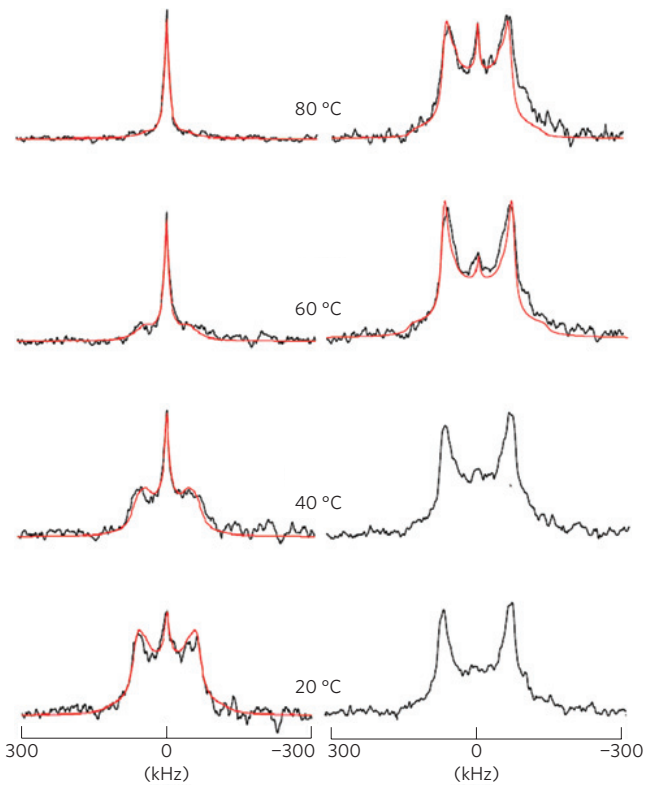

Figure 6 | Adsorbed imidazoles in 1 have a higher mobility than that of 2 in the whole range of temperature. ^{2}H solid-state NMR spectra of **1** ⊃ Im-d_4 (left) and **2** ⊃ Im-d_4 (right). The simulation results are shown as red lines.

measured temperature of 20 °C, we observed a clear Pake-type doublet pattern with a splitting width of 120 kHz, indicating that the adsorbed imidazole-d_4 behaves totally anisotropically. As the temperature increases, a narrow Lorentzian-type peak appears in the middle of the anisotropic powder pattern, corresponding to the emergence of isotropic imidazole by thermal activation. There are two possible explanations for the spectrum: the first is that free motional imidazole with low frequency shows a narrow peak and the second is the simultaneous coexistence of frequencies of slow and fast imidazole. Nonetheless, the spectrum at 40 °C indicates the existence of activated guests in pores and the relative intensity of the activated species increases as the temperature increases to 80 °C.

In the case of **1** ⊃ Im, spectra also show doublet powder patterns at low temperatures (−20 and −60 °C) with the same splitting width as in **2** ⊃ Im at temperatures lower than 30 °C. However, a narrow Lorentzian-type peak starts to appear at 20 °C. This clearly indicates that at ambient temperature the imidazole in **1** can show isotropic motion with a larger frequency than **2**. The fraction of isotropic imidazole becomes dominant at 40 °C and at 80 °C we can no longer observe any Pake-doublet pattern at all. This suggests that all adsorbed imidazole within the pores of **1** has a fast isotropic motion. Using the NMR line shapes obtained, we evaluated the motion of the imidazole using a simulation procedure. We used a free rotation model of imidazole molecules with tetrahedral orientations as the main motion because this is associated with the Grotthus mechanism. We succeeded in obtaining theoretical patterns for both samples, at each temperature, on the basis of the tetrahedral free rotational model as shown in Fig. 6 and clearly observed that the rotation frequency of **1** is greater than that of **2**. For example, the frequency of **1** at 60 °C is 45 kHz, whereas that of **2** is 10 kHz, and the frequency of **1** at 20 °C (20 kHz) is still larger than that of **2** at 90 °C (18 kHz) (see Supplementary Fig. S2). Consequently, we are able to conclude that the degree of motional behaviour of the accommodated imidazole of **1** is greater than in the case of **2**, which strongly supports the difference in conductivity.

We have presented a new approach to create proton transportation space on the basis of the use of proton-carrier organic molecules to enhance the proton conductivity of solid materials under anhydrous conditions at high temperature. The different values of conductivity of imidazole in compounds **1** and **2** are consistent with the dynamic properties of imidazole adsorbed in the pores. The hydrophilic microporous surface of **2** results in a strong interaction with even half the amount of adsorbed imidazoles and significantly decelerates their mobility, resulting in a poor proton-transfer rate. On the other hand, because of the hydrophobic and flat pore surface of **1**, adsorbed imidazole can move more freely than in **2** and than in the bulk phase and we eventually observe higher proton conductivity, which is comparable to that of a conventional organic polymer conductor such as poly(4-vinylimidazole) (ref. 48). PCP can provide an appropriate pore environment and size for the target proton carrier by the fine-tuning of their components. In other words, the optimum mobility and density of proton carriers can be reached by taking advantage of the designability of PCPs. The strategy would be considered significant to prepare hybrid materials with high proton conductivity.

Methods

Materials. Aluminium(III) nitrate nanohydrate $Al(NO_3)_3 \cdot 9H_2O$ (WAKO, 99.9%); terephthalic acid $HO_2C–(C_6H_4)–CO_2H$ (WAKO, 95%); 1,4-naphthalene dicarboxylic acid $HO_2C–(C_{10}H_8)–CO_2H$ (WAKO, 95%); imidazole (WAKO, 99%) and imidazole (D-4, CIL, 98%) were used as received. Distilled water was used.

Synthesis of {Al(μ_2-OH)(1,4-ndc)}$_n$ (1). A mixture of $Al(NO_3)_3 \cdot 9H_2O$ (0.375 g, 1.0 mmol); 1,4-naphthalene dicarboxylic acid (0.108 g, 0.5 mmol) and deionized water (10 ml) was placed in a 23 ml Teflon autoclave and heated at 180 °C for one day. The initial pH of the reaction mixture was 2.5 and the final pH was 2.0. After filtering and washing the crude product with distilled water, a pure, light-yellow powder of **1** · $2H_2O$ was obtained (yield 80%). The sample was evacuated at 150 °C for 12 h to afford the guest-free compound **1**

Synthesis of {Al(μ_2-OH)(1,4-bdc)}$_n$ (2). The synthesis of **2** was carried out under hydrothermal conditions using $Al(NO_3)_3 \cdot 9H_2O$ (1.30 g, 3.5 mmol), 1,4-benzenedicarboxylic acid (0.288 g, 2.5 mmol) and distilled water (10 ml). The reaction was carried out in a 23 ml Teflon autoclave. The reaction mixture was heated at 220 °C for three days. After filtering and washing with distilled water, a white powder was obtained. It was identified by powder X-ray diffraction analysis. The excess terephthalic acid in the pores was removed by high-temperature treatment at 330 °C for three days. XRPD analysis revealed that the material was the guest-free compound **2**.

Preparation of imidazole-loaded frameworks. Products **1** and **2** were again degassed by heating to 120 °C under reduced pressure for 12 h to remove guest molecules. Imidazole was vapourized into guest-free **1** and **2** at 120 °C, overnight, to yield **1** ⊃ Imi and **2** ⊃ Imi. XRPD patterns of both these compounds confirmed that the frameworks were maintained. The amount of loaded imidazole was determined by thermogravimetric analysis.

Proton conductivity measurement of 1 ⊃ Im and 2 ⊃ Im. Samples for conductivity measurements were prepared by sandwiching the respective powders **1** ⊃ Im and **2** ⊃ Im between two gold-coated electrodes (diameter 3 mm) and then tightly connecting the two electrodes, by means of springs, to ensure good contact between the sample and each electrode. Temperature-dependent conductivities of **1** ⊃ Im and **2** ⊃ Im were determined using a.c. impedance spectroscopy (Solartron SI 1260 Impedance/Gain-Phase analyser), using a homemade cell over the frequency range 1 Hz–10 MHz and with an input voltage amplitude of 100 mV. The measurement cell was filled with nitrogen at atmospheric pressure before recording the measurements. ZView software was used to extrapolate impedance data results by means of an equivalent circuit simulation to complete the Nyquist plot and obtain the resistance values.

^{2}H solid-state NMR. Solid-state ^{2}H NMR spectra were recorded using a Varian Chemagnetics CMX-300 spectrometer, at 45.826 MHz and a quadrupole echo pulse sequence. Simulated spectra were produced with FORTRAN programs written by us.

Received 20 November 2008; accepted 30 July 2009; published online 6 September 2009

References

1. Kreuer, K. D., Paddison, S. J., Spohr, E. & Schuster, M. Transport in proton conductors for fuel-cell applications: Simulations, elementary reactions, and phenomenology. *Chem. Rev.* **104,** 4637–4678 (2004).
2. Schuster, M. F. H. & Meyer, W. H. Anhydrous proton-conducting polymers. *Annu. Rev. Mater. Res.* **33,** 233–261 (2003).
3. Jannasch, P. Recent developments in high-temperature proton conducting polymer electrolyte membranes. *Curr. Opin. Colloid Interface Sci.* **8,** 96–102 (2003).
4. Li, S. *et al.* Synthesis and properties of imidazole-grafted hybrid inorganic–organic polymer membranes. *Electrochim. Acta* **51,** 1351–1358 (2006).
5. West, A. R. *Basic Solid State Chemistry* (Wiley, 1999).
6. Kawada, A., McGhie, A. R. & Labes, M. M. Protonic conductivity in imidazole single crystal. *J. Chem. Phys.* **52,** 3121–3125 (1970).
7. Noro, S., Kitagawa, S., Kondo, M. & Seki, K. A new, methane adsorbent, porous coordination polymer. *Angew. Chem. Int. Ed.* **39,** 2081–2084 (2000).
8. Rowsell, J. L. & Yaghi, O. M. Strategies for hydrogen storage in metal-organic frameworks. *Angew. Chem. Int. Ed.* **44,** 4670–4679 (2005).
9. Ferey, G. *et al.* Hydrogen adsorption in the nanoporous metal-benzenedicarboxylate $M(OH)(O_2C–C_6H_4–CO_2)(M = Al^{3+}, Cr^{3+})$, MIL-53. *Chem. Commun.* 2976–2977 (2003).
10. Rosi, N. L. *et al.* Hydrogen storage in microporous metal-organic frameworks. *Science* **300,** 1127–1129 (2003).
11. Li, H., Eddaoudi, M., O'Keeffe, M. & Yaghi, O. M. Design and synthesis of an exceptionally stable and highly porous metal-organic framework. *Nature* **402,** 276–279 (1999).
12. Cychosz, K. A., Wong-Foy, A. G. & Matzger, A. J. Liquid phase adsorption by microporous coordination polymers: Removal of organosulfur compounds. *J. Am. Chem. Soc.* **130,** 6938–6939 (2008).
13. Finsy, V. *et al.* Pore-filling-dependent selectivity effects in the vapor-phase separation of xylene isomers on the metal-organic framework MIL-47. *J. Am. Chem. Soc.* **130,** 7110–7118 (2008).
14. Bradshaw, D. *et al.* Permanent microporosity and enantioselective sorption in a chiral open framework. *J. Am. Chem. Soc.* **126,** 6106–6114 (2004).
15. Dybtsev, D. N. *et al.* Microporous manganese formate: A simple metal-organic porous material with high framework stability and highly selective gas sorption properties. *J. Am. Chem. Soc.* **126,** 32–33 (2004).
16. Min, K. S. & Suh, M. P. Self-assembly and selective guest binding of three-dimensional open-framework solids from a macrocyclic complex as a trifunctional metal building block. *Chem. Eur. J.* **7,** 303–313 (2001).
17. Wang, B. *et al.* Colossal cages in zeolitic imidazolate frameworks as selective carbon dioxide reservoirs. *Nature* **453,** 207–211 (2008).
18. Hasegawa, S. *et al.* Three-dimensional porous coordination polymer functionalized with amide groups based on tridentate ligand: Selective sorption and catalysis. *J. Am. Chem. Soc.* **129,** 2607–2614 (2007).
19. Horike, S., Dinca, M., Tamaki, K. & Long, J. R. Size-selective lewis acid catalysis in a microporous metal-organic framework with exposed Mn^{2+} coordination sites. *J. Am. Chem. Soc.* **130,** 5854–5855 (2008).
20. Cho, S.-H. *et al.* A metal-organic framework material that functions as an enantioselective catalyst for olefin epoxidation. *Chem. Commun.* **24,** 2563–2565 (2006).
21. Horcajada, P. *et al.* Synthesis and catalytic properties of MIL-100(Fe), an iron(III) carboxylate with large pores. *Chem. Commun.* 2820–2822 (2007).
22. Schroder, F. *et al.* Ruthenium nanoparticles inside porous $[Zn_4O(bdc)_3]$ by hydrogenolysis of adsorbed [Ru(cod)(cot)]: A solid-state reference system for surfactant-stabilized ruthenium colloids. *J. Am. Chem. Soc.* **130,** 6119–6130 (2008).
23. Ingleson, M. J. *et al.* Generation of a solid Bronsted acid site in a chiral framework. *Chem. Commun.* 1287–1289 (2008).
24. Fujita, M., Kwon, Y. J., Washizu, S. & Ogura, K. Preparation, clathration ability, and catalysis of a two-dimensional square network material composed of cadmium(II) and 4,4′ − bipyridine. *J. Am. Chem. Soc.* **116,** 1151–1152 (1994).
25. Seo, J. S. *et al.* A homochiral metal-organic porous material for enantioselective separation and catalysis. *Nature* **404,** 982–986 (2000).
26. Evans, O. R., Ngo, H. L. & Lin, W. Chiral porous solids based on lamellar lanthanide phosphonates. *J. Am. Chem. Soc.* **123,** 10395–10396 (2001).
27. Ferey, G. *et al.* Mixed-valence Li/Fe-based metal-organic frameworks with both reversible redox and sorption properties. *Angew. Chem. Int. Ed.* **46,** 3259–3263 (2007).
28. Kitagawa, H. *et al.* Highly proton-conductive copper coordination polymer, H2dtoaCu (H2dtoa=dithiooxamide anion). *Inorg. Chem. Commun.* **6,** 346–348 (2003).
29. Sadakiyo, M., Yamada, T. & Kitagawa, H. Rational designs for highly proton-conductive metal-organic frameworks. *J. Am. Chem. Soc.* **131,** 9906–9907 (2009).
30. Uemura, T. *et al.* Radical polymerisation of styrene in porous coordination polymers. *Chem. Commun.* 5968–5970 (2005).
31. Uemura, T. *et al.* Conformation and molecular dynamics of single polystyrene chain confined in coordination nanospace. *J. Am. Chem. Soc.* **130,** 6781–6788 (2008).
32. Mulfort, K. L. & Hupp, J. T. Chemical reduction of metal-organic framework materials as a method to enhance gas uptake and binding. *J. Am. Chem. Soc.* **129,** 9604–9605 (2007).
33. Muller, M. *et al.* Loading of MOF-5 with Cu and ZnO nanoparticles by gas-phase infiltration with organometallic precursors: Properties of Cu/ZnO@MOF-5 as catalyst for methanol synthesis. *Chem. Mater.* **20,** 4576–4587 (2008).
34. Turner, S. *et al.* Direct imaging of loaded metal-organic framework materials (Metal@MOF-5). *Chem. Mater.* **20,** 5622–5627 (2008).
35. Horcajada, P. *et al.* Flexible porous metal-organic frameworks for a controlled drug delivery. *J. Am. Chem. Soc.* **130,** 6774–6780 (2008).
36. Horcajada, P. *et al.* Metal-organic frameworks as efficient materials for drug delivery. *Angew. Chem. Int. Ed.* **45,** 5974–5978 (2006).
37. Tanaka, D. *et al.* Anthracene array-type porous coordination polymer with host–guest charge transfer interactions in excited states. *Chem. Commun.* 3142–3144 (2007).
38. Comotti, A. *et al.* Nanochannels of two distinct cross-sections in a porous Al-based coordination polymer. *J. Am. Chem. Soc.* **130,** 13664–13672 (2008).
39. Loiseau, T. *et al.* A rationale for the large breathing of the porous aluminum terephthalate (MIL-53) upon hydration. *Chem. Eur. J.* **10,** 1373–1382 (2004).
40. Serre, C. *et al.* An explanation for the very large breathing effect of a metal-organic framework during CO_2 adsorption. *Adv. Mater.* **19,** 2246–2251 (2007).
41. Spek, A. L. Single-crystal structure validation with the program PLATON. *J. Appl. Crystallogr.* **36,** 7–13 (2003).
42. Craven, B. M., McMullan, R. K., Bell, J. D. & Freeman, H. C. The crystal structure of imidazole by neutron diffraction at 20 °C and −150 °C. *Acta Crystallogr. B* **33,** 2585–2589 (1977).
43. Horike, S. *et al.* Motion of methanol adsorbed in porous coordination polymer with paramagnetic metal ions. *Chem. Commun.* 2152–2153 (2004).
44. Ueda, T. *et al.* Phase transition and molecular motion of cyclohexane confined in metal-organic framework, IRMOF-1, as studied by 2H NMR. *Chem. Phys. Lett.* **443,** 293–297 (2007).
45. Horike, S. *et al.* Dynamic motion of building blocks in porous coordination polymers. *Angew. Chem. Int. Ed.* **45,** 7226–7230 (2006).
46. Schmidt-Rohr, K. & Spiess, H. W. *Multidimensional Solid-State NMR and Polymers* (Academic, 1994).
47. Abragam, A. *Principles of Nuclear Magnetism* (Oxford Univ. Press, 1961).
48. Bozkurt, A. & Meyer, W. H. Proton conducting blends of poly(4-vinylimidazole) with phosphoricacid. *Solid State Ion.* **138,** 259–265 (2001).

Acknowledgements

This work was supported by Japan Science and Technology Agency (JST).

Author contributions

S.B. and M.H. prepared the aluminium PCPs. S.B. and T.K. measured the ionic conductivity. S.B., N.Y. and D.T. carried out solid-state NMR work and their data analysis was carried out by S.B. and M.M. The work was directed by S.K., and S.B. and S.H. contributed in writing the manuscript.

Additional information

Supplementary information accompanies this paper on www.nature.com/naturematerials. Reprints and permissions information is available online at http://npg.nature.com/reprintsandpermissions. Correspondence and requests for materials should be addressed to S.K.